

## Article

# A Highly Active Porous Mo<sub>2</sub>C-Mo<sub>2</sub>N Heterostructure on Carbon Nanowalls/Diamond for a High-Current Hydrogen Evolution Reaction

Zhaofeng Zhai <sup>1,2</sup>, Chuyan Zhang <sup>1</sup>, Bin Chen <sup>1,2</sup>, Lusheng Liu <sup>1</sup>, Haozhe Song <sup>1</sup>, Bing Yang <sup>1,2</sup>, Ziwen Zheng <sup>1,2</sup>, Junyao Li <sup>1</sup>, Xin Jiang <sup>1,3,\*</sup>  and Nan Huang <sup>1,2,\*</sup>

- <sup>1</sup> Shenyang National Laboratory for Materials Science (SYNL), Institute of Metal Research (IMR), Chinese Academy of Sciences (CAS), No. 72 Wenhua Road, Shenyang 110016, China; zfzhai@imr.ac.cn (Z.Z.); zhangcy@imr.ac.cn (C.Z.); bchen18s@imr.ac.cn (B.C.); lsliu@imr.ac.cn (L.L.); hzsong@imr.ac.cn (H.S.); byang@imr.ac.cn (B.Y.); zwzheng21s@imr.ac.cn (Z.Z.); ljy2464011899@163.com (J.L.)
- <sup>2</sup> School of Materials Science and Engineering, University of Science and Technology of China, No. 72 Wenhua Road, Shenyang 110016, China
- <sup>3</sup> Institute of Materials Engineering, University of Siegen, No. 9-11 Paul-Bonatz-Str., 57076 Siegen, Germany
- \* Correspondence: xjiang@imr.ac.cn (X.J.); nhuang@imr.ac.cn (N.H.)

**Abstract:** Developing non-precious metal-based electrocatalysts operating in high-current densities is highly demanded for the industry-level electrochemical hydrogen evolution reaction (HER). Here, we report the facile preparation of binder-free Mo<sub>2</sub>C-Mo<sub>2</sub>N heterostructures on carbon nanowalls/diamond (CNWs/D) via ultrasonic soaking followed by an annealing treatment. The experimental investigations and density functional theory calculations reveal the downshift of the d-band center caused by the heterojunction between Mo<sub>2</sub>C/Mo<sub>2</sub>N triggering highly active interfacial sites with a nearly zero  $\Delta G_{H^*}$  value. Furthermore, the 3D-networked CNWs/D, as the current collector, features high electrical conductivity and large surface area, greatly boosting the electron transfer rate of HER occurring on the interfacial sites of Mo<sub>2</sub>C-Mo<sub>2</sub>N. Consequently, the self-supporting Mo<sub>2</sub>C-Mo<sub>2</sub>N@CNWs/D exhibits significantly low overpotentials of 137.8 and 194.4 mV at high current densities of 500 and 1000 mA/cm<sup>2</sup>, respectively, in an alkaline solution, which far surpass the benchmark Pt/C (228.5 and 359.3 mV) and are superior to most transition-metal-based materials. This work presents a cost-effective and high-efficiency non-precious metal-based electrocatalyst candidate for the electrochemical hydrogen production industry.

**Keywords:** hydrogen evolution reaction; high current density; carbon nanowalls; diamond; Mo<sub>2</sub>C; Mo<sub>2</sub>N; heterostructure



**Citation:** Zhai, Z.; Zhang, C.; Chen, B.; Liu, L.; Song, H.; Yang, B.; Zheng, Z.; Li, J.; Jiang, X.; Huang, N. A Highly Active Porous Mo<sub>2</sub>C-Mo<sub>2</sub>N Heterostructure on Carbon Nanowalls/Diamond for a High-Current Hydrogen Evolution Reaction. *Nanomaterials* **2024**, *14*, 243. <https://doi.org/10.3390/nano14030243>

Academic Editor: Jooheon Kim

Received: 15 December 2023

Revised: 7 January 2024

Accepted: 16 January 2024

Published: 23 January 2024



**Copyright:** © 2024 by the authors. Licensee MDPI, Basel, Switzerland. This article is an open access article distributed under the terms and conditions of the Creative Commons Attribution (CC BY) license (<https://creativecommons.org/licenses/by/4.0/>).

## 1. Introduction

Hydrogen energy, characterized by cleanliness and high energy density, is emerging as a sustainable alternative to fossil fuels [1,2]. The electrochemical hydrogen evolution reaction (HER) holds significant promise for large-area green hydrogen production, offering a solution to the high carbon emissions associated with the traditional steam reforming technique, due to the advantages of utilizing an exhaustless and cost-effective water resource, zero carbon emission, and ensuring high purity (>95%) [3–5]. Achieving this industrial goal requires highly active and inexpensive HER electrocatalysts capable of operating at high current density ( $\geq 500$  mA/cm<sup>2</sup>) [1,6,7]. While Pt-based materials are regarded as excellent HER electrocatalysts, they suffer from the penalty of scarcity and a high cost [8]. Therefore, it is highly required to develop efficient non-precious metal alternatives for high-current HER applications.

As non-precious-metal electrocatalysts, Mo<sub>2</sub>C-based nanostructures have provoked significant attention from researchers due to their earth abundance, low cost, analogous d-orbital electronic structure to the Pt, and good resistance to dissolution [9–11]. However,

the high d-band center position of the Mo site in the Mo<sub>2</sub>C induces a strong hydrogen-binding that is detrimental to the desorption process and consequently resulting in an unsatisfactory HER activity [12,13]. For instance, Chi et al. demonstrated that a large overpotential of 189 mV is required for the Mo<sub>2</sub>C nanospheres to reach a current density of 10 mA/cm<sup>2</sup> in 1 M KOH [14]. To overcome the sluggish reaction kinetics, heteroatom doping with either nonmetals, such as N [15] and P [16], or metals, such as Ni [17] and Co [18], into the Mo<sub>2</sub>C as well as the design of heterostructures [19,20] have been employed to create a modulation of the electronic structure and boost the intrinsic HER activity. In this context, a Mo<sub>2</sub>C-Mo<sub>2</sub>N heterostructure was prepared by calcining Mo-containing polyoxometalates and graphene oxide in a NH<sub>3</sub> atmosphere and exhibited an optimized overpotential of 154 mV in 1 M KOH [21]. Recently, a lower overpotential of 88.1 mV at 10 mA/cm<sup>2</sup> was reported based on a ZIF-67-derived Mo<sub>2</sub>C-Mo<sub>2</sub>N catalyst [22]. It is verified that the construction of a heterostructure is a viable and efficient way to improve HER performance. Nevertheless, most studies focus on the HER characteristics at low current density, e.g., 10 and 100 mA/cm<sup>2</sup>, which falls short of addressing the practical application at high current operation [23,24]. In addition, in the case of above nanoparticle-type electrocatalysts, binders were needed to immobilize the particles onto a current collector, which possesses, however, several drawbacks, such as restricting exposure of the active sites, impeding mass transport, and obstructing electron transfer that reduce the overall HER performance [25,26].

In this study, we prepared binder-free porous Mo<sub>2</sub>C-Mo<sub>2</sub>N heterostructures on the carbon-nanowalls/diamond-coated carbon cloth (Mo<sub>2</sub>C-Mo<sub>2</sub>N@CNWs/D) via facile soaking in an ammonium molybdate solution followed by annealing with melamine. In this self-supporting electrocatalyst, the carbon nanowalls/diamond (CNWs/D), with a high electrical conductivity, open accessible surface, and large specific area, serves as a template for depositing Mo<sub>2</sub>C-Mo<sub>2</sub>N, efficiently enlarging the electrically active surface area (ECSA), as well as a current collector, greatly facilitating the electron transfer during HER. An electrochemically active Mo<sub>2</sub>C-Mo<sub>2</sub>N heterostructure is finely tuned in phase constituents to attain optimum HER characteristics. Density functional theory (DFT) calculations further reveal that the atoms located at the Mo<sub>2</sub>C-Mo<sub>2</sub>N interface possess greatly enhanced intrinsic activity. Derived from the excellent current collector and the boosted intrinsic activity, consequently, much lower overpotentials at both low (10 mA/cm<sup>2</sup>) and high current densities (500 and 1000 mA/cm<sup>2</sup>) are achieved on Mo<sub>2</sub>C-Mo<sub>2</sub>N@CNWs/D in 1 M KOH. This work provides a facile methodology for the construction of a non-precious electrocatalyst and promising applications in electrochemical high-current hydrogen production.

## 2. Materials and Methods

### 2.1. Material Preparation

CNW<sub>5</sub>/D film was prepared on carbon cloth (CC) using microwave plasma chemical vapor deposition (MPCVD) with a 915 MHz reactor (Cyrannus, Iplas Innovative Plasma Systems GmbH, Troisdorf, Germany). The CC was ultrasonically cleaned in acetone, ethanol, water, and nitric acid, followed by being ultrasonically seeded in the diamond suspension for 30 min. It was verified that the diamond seed enhanced the growth rate and robustness of carbon nanowalls (CNWs). The seeded CC was then placed onto the Al<sub>2</sub>O<sub>3</sub> holder in the MPCVD chamber. During the deposition, a microwave power of 6 kW, a H<sub>2</sub> flow rate of 200 sccm, a CH<sub>4</sub> flow rate of 14 sccm, and a chamber pressure of ~30 mbar were employed. The substrate temperature was estimated to be ~1065 °C, monitored using an infrared pyrometer. After 60 min of growth, the plasma was shut down and the pristine CNWs/D film was obtained on the CC.

The preparation of Mo<sub>2</sub>C-Mo<sub>2</sub>N@CNW<sub>5</sub>/D involved soaking CNW<sub>5</sub>/D in a Mo-containing solution and thermal treatment with melamine. Before the soaking, the pristine CNW<sub>5</sub>/D film surface was modified to become O-terminated through UV irradiation in the air, in order to impart a hydrophilic property in an aqueous solution. After soaking for 30 min in an ultrasonic bath made up of 31.39 wt% (NH<sub>4</sub>)<sub>6</sub>Mo<sub>7</sub>O<sub>24</sub> (Sinopharm

Chemical Reagent Co., Ltd., AR, Shanghai, China), the obtained Mo precursor@CNW<sub>5</sub>/D was annealed with 0.2 of melamine (Aladdin, 99%) positioned upstream at a heat rate of 2 °C/min in an Ar/H<sub>2</sub> atmosphere. According to the annealing temperature (including 500, 650, 700, 750, 800, and 850 °C), the obtained electrocatalysts are designated as Mo<sub>2</sub>C-Mo<sub>2</sub>N@CNW<sub>5</sub>/D-500, -650, -700, -750, -800, and -850, respectively. For comparison, Mo<sub>2</sub>C@CNW<sub>5</sub>/D-650 was prepared using the same routine at 650 °C, albeit without the introduction of melamine. Mo<sub>2</sub>C-Mo<sub>2</sub>N@CC-650 was prepared on CC using a similar routine at 650 °C.

## 2.2. Material Characterization

The morphology and elemental composition were investigated by using a field-emission scanning electron microscope (SEM, Hitachi, SU 70, Tokyo, Japan). The micro-XRD (Bruker, D8 Discover, Billerica, MA, USA) using a Co K $\alpha$ <sub>1</sub> radiation source ( $\lambda = 1.78897 \text{ \AA}$ ) was employed to obtain the phase information. In addition, the carbon phase of CNW<sub>5</sub>/D was studied using a Raman spectroscopy (Horiba, Labram HR Evolution instrument, Kyoto, Japan) based on a 532 nm laser. The microstructure and elemental mapping distribution were characterized by using a transmission electron microscope (TEM, ThermoFisher, Talos F200X, Waltham, MA, USA) equipped with an energy dispersive X-ray spectrometer (EDS, ThermoFisher, Super X G2, Waltham, MA, USA).

To access the surficial chemical state, X-ray photoelectron spectra (XPS) were recorded by using a Thermo ESCALAB Xi<sup>+</sup> instrument (Waltham, MA, USA) with an Al K $\alpha$  source ( $h\nu = 1486.6 \text{ eV}$ ). The bare surface of Mo<sub>2</sub>C-Mo<sub>2</sub>N@CNW<sub>5</sub>/D was measured without sputtering. In addition, during the XPS test, the power was 150 W, and the electron emission angle was 55°. The analyzed area had a diameter of 500  $\mu\text{m}$ . The base pressure was  $2.77 \times 10^{-7}$  mbar. The charge neutralizer was used to reduce the possibility that the sample charges up. Furthermore, all the acquired XPS data were corrected based on the highest peak located at 284.6, assigned to the adventitious carbon contamination [27]. To reveal the chemical state of Mo, C, and N species of Mo<sub>2</sub>C-Mo<sub>2</sub>N@CNW<sub>5</sub>/D, peak fitting was conducted further using XPSPEAK software (Version 4.1) based on the acquired XPS spectra. All spectra were fitted with Shirley backgrounds and the Voigt function (80% Gaussian and 20% Lorentzian). For the Mo 3d fitting, the 3d<sub>3/2</sub>/3d<sub>5/2</sub> area ratio was constrained at around 0.66. In addition, the XPS fitting conformed to the criterion of qualitative self-consistency [27].

## 2.3. Electrochemical Measurements

Electrocatalytic HER measurement of all samples was carried out on an electrochemical workstation (Metrohm, PGSTAT302N, Herisau, Switzerland) in a three-electrode cell at room temperature. The three-electrode system was composed of a self-supporting working electrode, a graphite rod counter electrode, and a Hg/HgO (1 M KOH) reference electrode. The measured potential was converted to a reversible hydrogen electrode (RHE) using the following equation:

$$E_{\text{RHE}} = E_{\text{Hg/HgO}} + 0.098 + 0.0591 \times \text{pH} \quad (1)$$

Linear sweep voltammetry (LSV) was carried out at the scan rate of 0.002 V/s to evaluate the overpotential and Tafel slope during the HER process. Cyclic voltammetry (CV) was performed at various scan rates ranging from 0.04 to 0.12 V/s to estimate the ECSA of the electrocatalyst. In addition, electrochemical impedance spectroscopy (EIS) was recorded at an overpotential of 74.6 mV with a 10 mV amplitude in the frequency range from 100 kHz to 0.1 Hz. Prior to the electrochemical test, Ar gas ( $\geq 99.999\%$ ) was bubbled into the electrolyte for 20 min to preclude the inference of the oxygen reduction reaction. All LSV potentials were demonstrated through a 95% *iR*-compensation based on the EIS results. All current densities were demonstrated after normalization using the geometric area of the electrocatalyst.

## 2.4. Calculation Method

DFT calculation was conducted using the plane-wave code implemented in the Vienna Ab Initio Simulation Package (VASP). The electron exchange and correlation are described with the generalized gradient approximation as parameterized by Perdew, Burke, and Ernzerhof (GGA-PBE), and the interaction between ions and electrons is described using the projector augmented wave method (PAW). The effective valence used here of each atom is 4.000 for the C atom, 5.000 for the N atom, and 6.000 for the Mo atom, respectively. For all calculations, the kinetic cut-off energy of 400 eV with the self-consistent field (SCF) tolerance of  $1 \times 10^{-6}$  eV and  $0.02 \text{ eV \AA}^{-1}$  was adopted. Figure S1 displays the side-view and top-view of the constructed model structure. Typically, the (111) crystal surface of  $\text{Mo}_2\text{N}$  and the (101) crystal surface of  $\text{Mo}_2\text{C}$  were chosen, consistent with the TEM and XRD results. To model the  $\text{Mo}_2\text{C}$ - $\text{Mo}_2\text{N}$  interface structure, we constructed firstly a supercell consisting of  $2 \times 3$   $\text{Mo}_2\text{C}$  (101) unit cells with  $2 \times 2$   $\text{Mo}_2\text{N}$  (111) unit cells in the vertical direction with a lattice mismatch of 0.3%. Then, the supercell was rotated  $90^\circ$  to expose the interface sites for subsequent adsorption energy calculations. A vacuum region of  $20 \text{ \AA}$  was set along the z direction to avoid the interaction between slabs. For the balance of the calculation accuracy and time cost, the k-point mesh was employed as  $3 \times 3 \times 1$  k-points for the structural relaxation and  $9 \times 9 \times 1$  for the energy band.

After the structural optimization, the adsorption free energy differences of  $\text{H}^*$  ( $\Delta G_{\text{H}^*}$ ) on different surface sites were determined as

$$\Delta G_{\text{H}^*} = \Delta E_{\text{H}^*} + \Delta ZPE - T\Delta S \quad (2)$$

where  $\Delta E_{\text{H}^*}$  is the energy change during the H adsorption/desorption process.  $\Delta ZPE$  and  $\Delta S$  are the difference in zero-point energy and entropy, respectively. T is the system temperature (298.15 K, in our calculation). For  $\text{H}^*$  on different surface sites, all 3N degrees of freedom are treated as vibrational motions while neglecting the contributions from the material surfaces. The  $\Delta G_{\text{H}^*}$  was calculated using *Vaspkit* software (Version 1.4.1) from  $\Delta E_{\text{H}^*}$ , temperature, pressure, and calculated vibrational energy [28].

## 3. Results and Discussion

### 3.1. Microstructure Characterizations

Figure 1 schematically shows the synthesis route of the  $\text{Mo}_2\text{C}$ - $\text{Mo}_2\text{N}$  heterostructure on the CNW/D-coated CC. Typically, the CNW<sub>5</sub>/D was initially deposited on the CC using the MPCVD system, followed by ultrasonic soaking in a  $(\text{NH}_4)_2\text{MoO}_4$  aqueous solution and then drying through centrifugation. Afterwards, the obtained Mo precursor@CNW<sub>5</sub>/D was immediately calcined with melamine in the Ar/H<sub>2</sub> atmosphere. Finally, the  $\text{Mo}_2\text{C}$ - $\text{Mo}_2\text{N}$ @CNW<sub>5</sub>/D was prepared. It is noteworthy that the proportion of  $\text{Mo}_2\text{C}$  to  $\text{Mo}_2\text{N}$  could be manipulated by varying the calcination temperature.

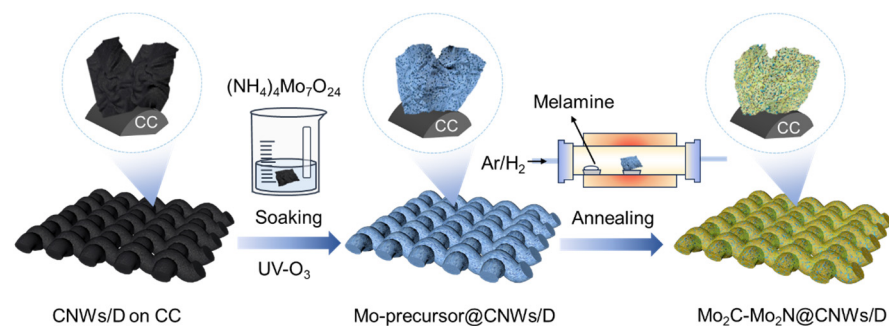


**Figure 1.** Schemic illustration for the preparation of  $\text{Mo}_2\text{C}$ - $\text{Mo}_2\text{N}$ @CNWs/D.

Figure 2a demonstrates the morphology of the CNW/D-coated CC. Compared to the smooth surface of bare CC (see Figure S2), the CNW/D-coated CC is completely surrounded by a furry 3D-networked nanowall after MPCVD. The magnified inset shows the nanowall

almost vertically aligned on the CC. In the Raman spectrum (Figure S3), well-separated peaks of the D band positioning at  $\sim 1344\text{ cm}^{-1}$ , the G band at  $\sim 1566\text{ cm}^{-1}$ , the D' band at  $\sim 1615\text{ cm}^{-1}$ , as well as the outstanding 2D band at  $\sim 2700\text{ cm}^{-1}$  are observed, and the  $I_D/I_G$  ratio is estimated to be 0.34. The  $I_D/I_G$  value is lower than the reported carbon nanofiber and highly branched graphene nanosheets [29,30], suggesting low-disordered CNWs were prepared on the CC substrate [31]. Figure 2b–g show the microstructure and constituent of the  $\text{Mo}_2\text{C-Mo}_2\text{N@CNW}_5/\text{D}$  after calcination. Notably, porous nanostructures completely cover the  $\text{CNW}_5/\text{D}$  (see Figure 2b). The CNWs/D, with an open accessible surface and large specific area, works as a great nano-template for the conformal growth of  $\text{Mo}_2\text{C-Mo}_2\text{N}$ . XRD measurement was used to determine the phases. As illustrated in Figure 2c, besides the predominated graphite peak, one can see two major characteristic peaks at  $44^\circ$  and  $46^\circ$ , matching well with the (111) plane of  $\text{Mo}_2\text{N}$  (PDF#25-1366) and (101) of  $\text{Mo}_2\text{C}$  (PDF#35-0787), respectively. This distinctly verifies that the  $\text{Mo}_2\text{C-Mo}_2\text{N}$  composite was rationally synthesized. In order to access deep insight into the microstructure, TEM characterizations were carried out on the  $\text{Mo}_2\text{C-Mo}_2\text{N@CNW}_5/\text{D}$ . Figure 2d illustrates that  $\text{Mo}_2\text{C-Mo}_2\text{N}$  has a porous structure. The pore size was estimated to be less than 10 nm, which can be clearly observed in the high-angle annular dark field (HAADF) TEM image in Figure S4. Figure 2e shows the high-resolution TEM image of  $\text{Mo}_2\text{C-Mo}_2\text{N}$ . As exhibited by the blue rectangle, the distances between adjacent lattice planes are measured to be 0.24 nm, consistent with the theoretical d-spacing of the {111} plane of  $\text{Mo}_2\text{N}$ . The fast-Fourier transformation pattern in the bottom-right panel also matches well with the  $\text{Mo}_2\text{N}$  diffracting spots taken along the [011] zone axis. Such results suggest that the  $\text{Mo}_2\text{N}$  (PDF#25-1366) phase constitutes the region  $ft_2$ . In addition, the measured interlayer spacing of 0.23 nm corresponding to the {101} plane of  $\text{Mo}_2\text{C}$  and the  $ft_1$  pattern related to the theoretical  $\text{Mo}_2\text{C}$  spots along the [011] zone indicate that the  $\text{Mo}_2\text{C}$  (PDF#35-0787) phase is obtained in the region  $ft_2$ . Importantly, an intimate interface is observed at the transition zone, hinting that a heterointerface is created between  $\text{Mo}_2\text{N}$  and  $\text{Mo}_2\text{C}$ . Due to the crystal lattice misfit, lattice distortion occurs at the heterointerface. It is believed that such distortion should induce an alteration in the local electronic structure, which accordingly manages the activity toward HER [32]. In addition, the CNWs, also designated as multilayered graphene with a lattice spacing of 0.35 nm, are obviously distinguished in the high-resolution TEM image taken near the edges (see Figure 2f). As an excellent current collector, CNWs support the  $\text{Mo}_2\text{C-Mo}_2\text{N}$  heterostructure, endowing high electrical conductivity to facilitate the transport of electrons generated during the HER into the electrochemical loop. Moreover, as shown in Figures 2g and S5, the HAADF image and corresponding EDS mapping images display a nearly even distribution of Mo, C, and N elements within the porous structure, suggesting the formation of abundant heterostructures in the catalyst.

All of the above results reveal that the porous  $\text{Mo}_2\text{C-Mo}_2\text{N}$  heterostructure was facilely fabricated on the  $\text{CNW}_5/\text{D}$ . Accounting for abundant active sites from porous  $\text{Mo}_2\text{C-Mo}_2\text{N}$  heterostructures and an excellent current collector from CNWs, an outstanding high-current HER performance is foreseen.

### 3.2. Performance of Hydrogen Evolution Reaction

The HER performance of the obtained  $\text{Mo}_2\text{C-Mo}_2\text{N@CNW}_5/\text{D}$  catalyst was investigated in 1 M KOH based on a typical three-electrode system. Figure S6 shows that the  $\text{Mo}_2\text{C-Mo}_2\text{N@CNW}_5/\text{D}$  prepared with the annealing time of 180 min demonstrates a better HER performance at high current densities than those with annealing times of 60 and 180 min. In the following, the effect of annealing temperature on the HER performance is investigated further. For comparison, the performance of the Pt/C@CC catalyst ( $2.0\text{ mg/cm}^2$ ) prepared using the drop-casting method and CC was also studied. As depicted in Figure 3a, the electrocatalytic performance of CC is very poor. Pt/C exhibits a high HER activity with an overpotential ( $\eta_{10}$ ) of 16.8 mV at a low current density of  $10\text{ mA/cm}^2$ . Comparatively, the  $\eta_{10}$  are measured to be 83.7, 42.8, 47.9, 62.6, 169.3, and 281.7 mV for the  $\text{Mo}_2\text{C-Mo}_2\text{N@CNW}_5/\text{D}$ -500, -650, -700, -750, -800, and -850. Table 1

lists the HER characteristics of these catalysts. Note that the overpotential gradually declines as the annealed temperature increases, reaches the minimum point of 42.8 mV for Mo<sub>2</sub>C-Mo<sub>2</sub>N@CNW<sub>5</sub>/D-650, and then goes up with elevating the temperature further.

To unveil the rate-determining step of the HER process, Figure 3b shows the Tafel plots derived from the LSV data. Pt/C@CC possesses the smallest Tafel slope estimated to be 32.5 mV/dec, consistent with the previously reported value of 31.0 mV/dec [33]. As the temperature increases, electrocatalysts demonstrate a similar variation trend in the Tafel slope as observed in the overpotential. As listed in Table 1, Mo<sub>2</sub>C-Mo<sub>2</sub>N@CNW<sub>5</sub>/D-650 has the smallest Tafel slope estimated to be 45.6 mV/dec. Generally, the HER occurring on the electrocatalyst involves the electrochemical adsorption of hydrogen (Volmer reaction), followed by either the electrochemical desorption (Heyrovsky reaction) or the chemical desorption (Tafel reaction) [34]. Given the Tafel slope of 120 mV/dec for the Volmer reaction-determining step, 30 mV/dec for the Tafel reaction, and 40 mV/dec for the Heyrovsky reaction, the HER mechanism closely adheres to the Heyrovsky mechanism on the Mo<sub>2</sub>C-Mo<sub>2</sub>N@CNW<sub>5</sub>/D-650. In contrast, other obtained electrocatalysts exhibit a mixed Volmer–Heyrovsky mechanism.

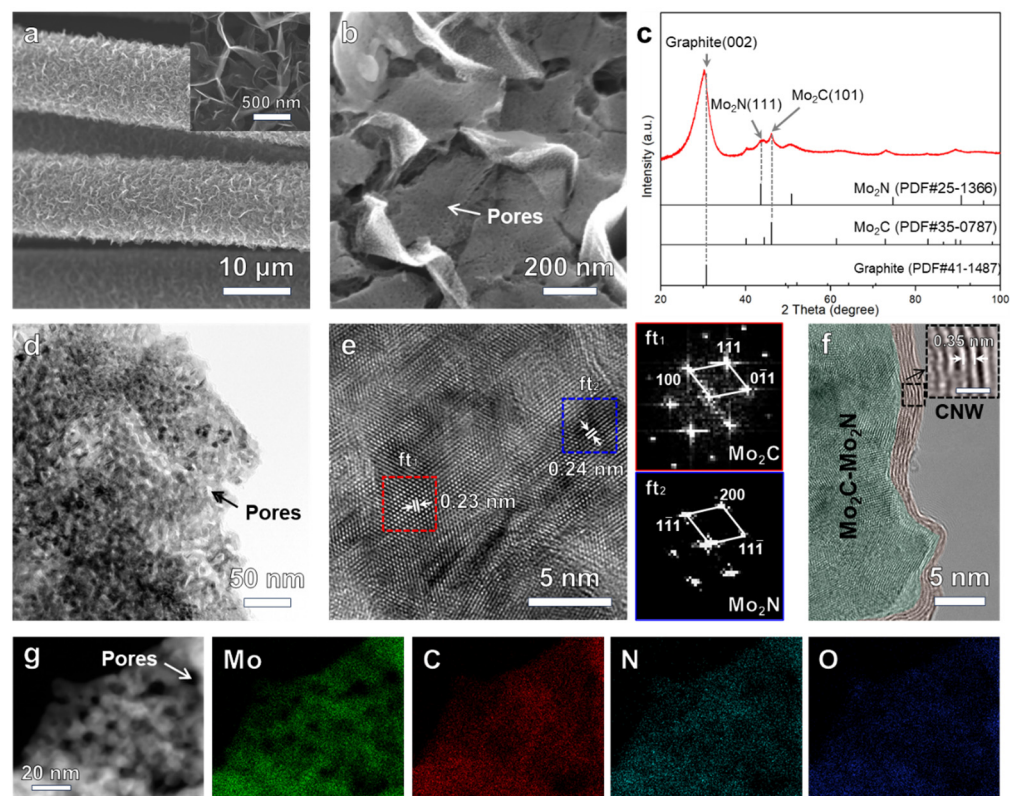


**Figure 2.** Microstructure characterizations of Mo<sub>2</sub>C-Mo<sub>2</sub>N@CNW<sub>5</sub>/D. (a) SEM image of the pristine CNW/D-coated CC. (b) SEM image and (c) XRD pattern of the Mo<sub>2</sub>C-Mo<sub>2</sub>N@CNW<sub>5</sub>/D. (d) Low-magnification and (e,f) high-resolution TEM images of Mo<sub>2</sub>C-Mo<sub>2</sub>N@CNW<sub>5</sub>/D. (g) HAADF TEM image and corresponding EDS elemental mapping images for Mo, C, N, and O of the Mo<sub>2</sub>C-Mo<sub>2</sub>N@CNW<sub>5</sub>/D.

To gain a comprehensive understanding of the charge transfer kinetics during the HER, EIS tests were carried out, and the Nyquist plots were recorded in Figure 3c. The curves are composed of a semicircle related to the electron transfer behavior on the active sites of the electrode [35]. The Mo<sub>2</sub>C-Mo<sub>2</sub>N@CNW<sub>5</sub>/D-650 demonstrates the smallest semicircle, and the charge transfer resistance ( $R_{ct}$ ) is calculated to be 8.59 Ω, derived from the fitting data using the Randles equivalent circuit (see Table 1). In addition, the ECSA of Mo<sub>2</sub>C-Mo<sub>2</sub>N@CNW<sub>5</sub>/D was estimated through the electrochemical double-layer capacitance

tests at different scan rates. As shown in Figure S7, no faradaic features are observed in these CV curves. Correspondingly, the capacitive current densities at  $\sim 0.23$  V were plotted as a function of the scan rate in Figure 3d. The electrochemical double-layer capacitance of  $\text{Mo}_2\text{C-Mo}_2\text{N@CNW}_5/\text{D-650}$  is the highest at  $891 \text{ mF/cm}^2$ , which then quickly decreases with the increase in the temperature.

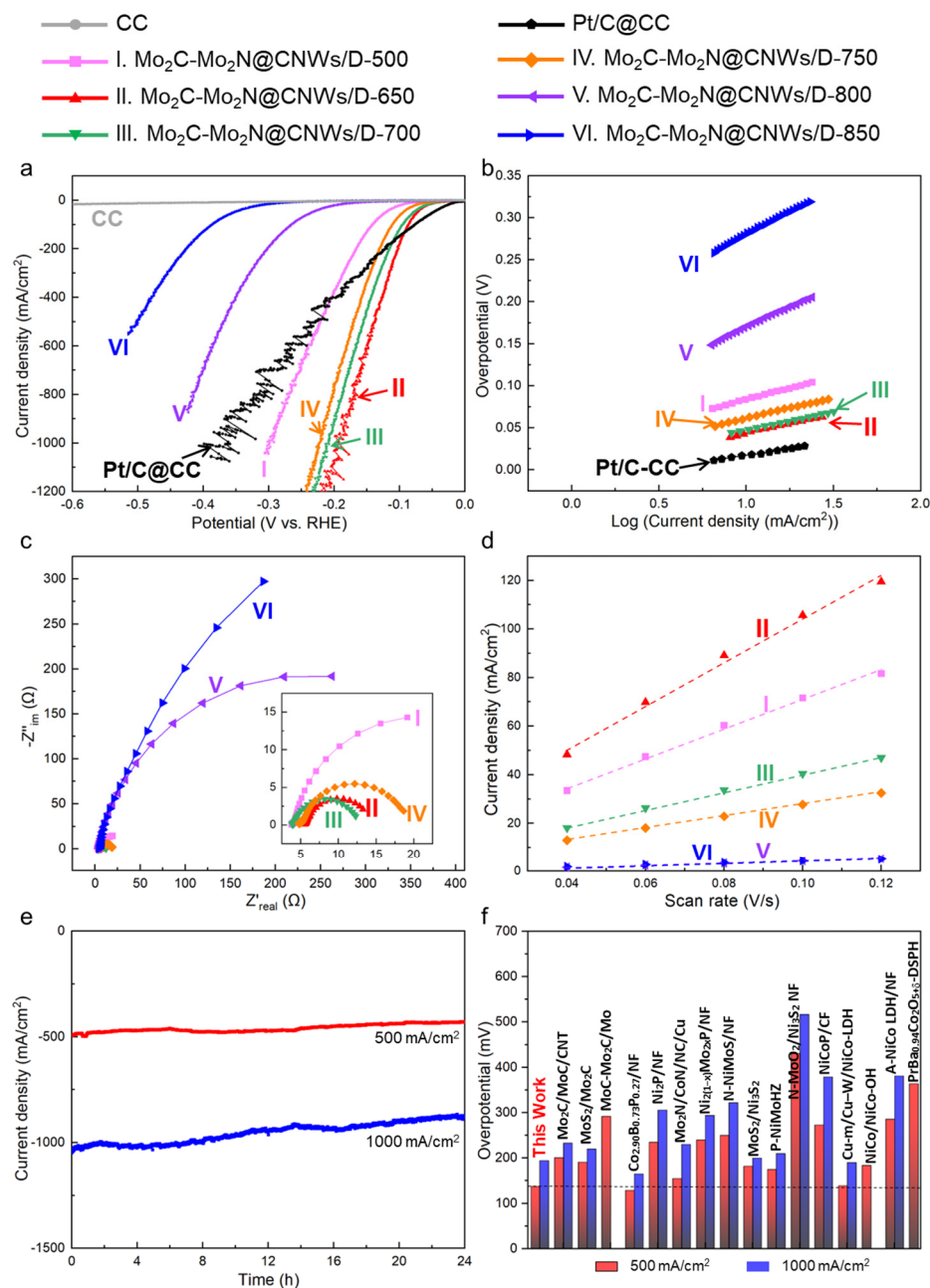


**Figure 3.** Electrocatalytic HER performance of  $\text{Mo}_2\text{C-Mo}_2\text{N@CNWs/D}$  in 1 M KOH. (a) Polarization curves and corresponding (b) Tafel plots. (c) Nyquist plots, and the inset showcases the Nyquist plots at high frequency. (d) Capacitive current variation as a function of scan rate from 0.04 to 0.12 V/s. (e) Long-term HER durability test of  $\text{Mo}_2\text{C-Mo}_2\text{N@CNWs/D-650}$  at high current densities. (f) Statistics histogram for the overpotential of our prepared  $\text{Mo}_2\text{C-Mo}_2\text{N@CNWs/D}$  and previously reported transition-metal-based electrocatalysts at 500 and 1000  $\text{mA/cm}^2$ . The curves of CC and Pt/C@CC catalyst are demonstrated in (a,b) as control.

**Table 1.** Electrocatalytic HER characteristics of Mo<sub>2</sub>C-Mo<sub>2</sub>N@CNWs/D-500, -650, -700, -750, -800, and -850. Pt/C@CC is included as control.

Sample	$\eta_{10}$ (mV)	$\eta_{500}$ (mV)	$\eta_{1000}$ (mV)	Tafel Slope (mV/dec)	$R_{ct}$ ( $\Omega$ )	Capacitance (mF/cm <sup>2</sup> )
Mo <sub>2</sub> C-Mo <sub>2</sub> N@CNWs/D-500	83.7	221.5	299.8	54.3	33.94	603
Mo <sub>2</sub> C-Mo <sub>2</sub> N@CNWs/D-650	42.8	137.8	194.4	45.6	8.59	891
Mo <sub>2</sub> C-Mo <sub>2</sub> N@CNWs/D-700	47.9	154.8	207.8	46.5	8.64	359
Mo <sub>2</sub> C-Mo <sub>2</sub> N@CNWs/D-750	62.6	169.4	222.9	48.8	13.95	243
Mo <sub>2</sub> C-Mo <sub>2</sub> N@CNWs/D-800	169.3	369.1	-	97.4	464.65	46
Mo <sub>2</sub> C-Mo <sub>2</sub> N@CNWs/D-850	281.7	502.2	-	109.2	1214.90	40
Pt/C@CC	16.8	228.5	359.3	32.5	-	-

Furthermore, the stability of Mo<sub>2</sub>C-Mo<sub>2</sub>N@CNWs/D-650 was determined through 24 h HER operation at high current densities. Figure 3e shows that the current density could retain 86.7% and 83.2% of the initial values at 500 and 1000 mA/cm<sup>2</sup>, respectively, suggesting the good stability of the Mo<sub>2</sub>C-Mo<sub>2</sub>N@CNWs/D electrocatalyst. In addition, Mo<sub>2</sub>C-Mo<sub>2</sub>N@CNWs/D-650 exhibits minor structural variations after 24 h HER operation at 500 mA/cm<sup>2</sup>, which implies the good structural stability (see Figure S8).

The above results demonstrate that the Mo<sub>2</sub>C-Mo<sub>2</sub>N@CNWs/D-650 exhibits the best performance, that is, the lowest overpotential ( $\eta_{10}$  = 42.8 mV), the lowest Tafel slope (45.6 mV/dec), the lowest  $R_{ct}$  (8.59  $\Omega$ ), and the largest capacitance (891 mF/cm<sup>2</sup>), among our prepared electrocatalysts. Furthermore, HER performances of the Mo<sub>2</sub>C-Mo<sub>2</sub>N@CNWs/D-650 and other reported transition-metal-based electrocatalysts are compared in Table 2. The  $\eta_{10}$  value is smaller than that of the reported molybdenum-based materials, such as Mo<sub>2</sub>C-Mo<sub>2</sub>N/HGr [21], Mo<sub>x</sub>C [13], P-MoP/Mo<sub>2</sub>N [36], Mo<sub>2</sub>C/MoC/CNT [20], and MoC-Mo<sub>2</sub>C/Mo [37]. More impressively, the Mo<sub>2</sub>C-Mo<sub>2</sub>N@CNWs/D-650 desires overpotentials of only 137.8 and 194.4 mV to achieve high current densities of 500 and 1000 mA/cm<sup>2</sup>, respectively. These values are much lower than those of benchmark Pt/C@CC ( $\eta_{500}$  = 228.5 mV,  $\eta_{1000}$  = 359.3 mV). Actually, Figure 3f and Table 2 verify that the Mo<sub>2</sub>C-Mo<sub>2</sub>N@CNWs/D-650 stands out as one of the most highly active electrocatalysts at high current density ( $\geq 500$  mA/cm<sup>2</sup>) in alkaline HER, compared with previously reported transition-metal-based materials [19,20,26,33,37–48].

**Table 2.** Comparison of the HER performance of transition-metal-based electrocatalysts in 1.0 M KOH solution.

Catalysts	$\eta_{10}$ (mV)	$\eta_{500}$ (mV)	$\eta_{1000}$ (mV)	Ref.
Mo <sub>2</sub> C-Mo <sub>2</sub> N@CNWs/D-650	42.8	137.8	194.4	This work
Mo <sub>2</sub> C-Mo <sub>2</sub> N/HGr	154	-	-	[21]
Mo <sub>x</sub> C	116	-	-	[13]
P-MoP/Mo <sub>2</sub> N	89	-	-	[36]
Mo <sub>2</sub> C/MoC/CNT	82	201	233	[20]
MoS <sub>2</sub> /Mo <sub>2</sub> C	-	191	220	[37]
MoC-Mo <sub>2</sub> C/Mo	98.2	292	-	[19]
Co <sub>2.90</sub> B <sub>0.73</sub> P <sub>0.27</sub> /NF	42	129	165	[38]
Ni <sub>2</sub> P/NF	-	235	306	[39]
Mo <sub>2</sub> N/CoN/NC/Cu	22	155	230	[26]
Ni <sub>2(1-x)</sub> Mo <sub>2x</sub> P/NF	72	240	294	[40]
N-NiMoS/NF	68	250	322	[41]
MoS <sub>2</sub> /Ni <sub>3</sub> S <sub>2</sub>	70	182	200	[33]
P-NiMoHZ	23	175	210	[42]
N-MoO <sub>2</sub> /Ni <sub>3</sub> S <sub>2</sub> NF	-	431	517	[43]
NiCoP/CF	47	273	379	[44]
Cu-m/Cu-W/NiCo-LDH	21	139	190	[45]
NiCo/NiCo-OH	19	184	-	[46]
A-NiCo LDH/NF	36	286	381	[47]
PrBa <sub>0.94</sub> Co <sub>2</sub> O <sub>5+<math>\delta</math></sub> -DSPH	186	364	-	[48]

### 3.3. Dependence of Hydrogen Evolution Reaction Performance on the Surface Chemical State

It is noteworthy that the electrocatalytic properties could be readily modulated by tuning the calcination temperature. As the temperature increases from 500 to 650 °C, the overpotential, Tafel slope, and  $R_{ct}$  of the catalysts demonstrate a decreasing trend. With elevating the temperature further until 850 °C, these HER characteristics all quickly increase.

To deeply understand such variation, the crystal phase and surface chemical state of Mo<sub>2</sub>C-Mo<sub>2</sub>N@CNW<sub>S</sub>/D are thoroughly studied. Figure S9 shows that the  $I_D/I_G$  of Mo<sub>2</sub>C-Mo<sub>2</sub>N@CNW<sub>S</sub>/D is estimated to be 0.53, slightly larger than that of bare CNW<sub>S</sub>/D. This indicates that defects are created in the CNWs through annealing treatment. The  $I_D/I_G$  value does not vary significantly as the annealing temperature increases. Figure 4a displays the XRD patterns of the catalysts prepared at different temperatures. The Mo<sub>2</sub>C-Mo<sub>2</sub>N@CNW<sub>S</sub>/D-500 sample shows a prominent peak positioned at ~43° and a feeble peak at 51°, corresponding to (202)/(020) of MoO<sub>2</sub> (PDF#73-1249) and (200) of Mo<sub>2</sub>N, respectively. Moving to 650° or above, distinct peaks associated with the Mo<sub>2</sub>C (101) and Mo<sub>2</sub>N (111) planes are clearly seen. The intensity ratio of the Mo<sub>2</sub>C (101) peak to Mo<sub>2</sub>N (111) peak is further calculated, and the results are recorded in Figure S10. Mo<sub>2</sub>C-Mo<sub>2</sub>N@CNW<sub>S</sub>/D-650 shows a ratio of 1.15, which then gradually rises with the increase in annealing temperature. It is deduced that Mo<sub>2</sub>N is easily fabricated at a low temperature. When a higher temperature was employed, more Mo<sub>2</sub>C was obtained in the Mo<sub>2</sub>C-Mo<sub>2</sub>N@CNW<sub>S</sub>/D.

The surface chemical states could play a crucial role in the HER as the electrochemical reaction primarily occurs at the surface sites. Figure S11 shows the XPS survey spectrum of Mo<sub>2</sub>C-Mo<sub>2</sub>N@CNW<sub>S</sub>/D-650, and the signals from C, N, Mo, and O are clearly distinguished. In comparison to the XPS survey before the HER test, all elements remain at the surface of Mo<sub>2</sub>C-Mo<sub>2</sub>N@CNW<sub>S</sub>/D-650 after the HER test (see Figure S12). This indicates a good chemical stability of the prepared electrocatalyst. Moreover, the high-resolution XPS spectra of C 1s, N 1s, and Mo 3d are deconvoluted and scrutinized in Figure 4b–d. In the C 1s spectrum, three peaks located at a binding energy of 283.47, 284.60, and 285.80 eV are attributed to C-Mo bonds in Mo<sub>2</sub>C, sp<sup>2</sup>-carbon bonds, and C-N bonds, respectively (see Figure 4b) [34,49]. The C-Mo species constitute 12.1 at% of the C species on the surface. The N 1s spectrum was deconvoluted into three components: the peak at 396.00 eV assigned to the N-Mo bond, the peak at 397.47 eV to pyridinic N, and the peak at 399.39 eV to pyrrolic N (see Figure 4c) [50]. The peak positioning at 394.60 eV is derived from Mo 3P bonds [21,50]. The N-Mo species make up 41.5 at% of the surface N species. It is noteworthy that the C 1s and N 1s investigations indicate the coexistence of Mo-C and Mo-N bonds on the surface of the catalyst. This is further confirmed by the high-resolution Mo 3d spectrum shown in Figure 4d. The Mo 3d spectrum reveals four deconvoluted doublets: peaks at 228.30 and 231.48 eV corresponding to the Mo-C bonds, peaks at 228.80 and 231.89 eV to the Mo-N bonds, peaks at 229.20 and 232.45 eV to the Mo<sup>4+</sup> species, and peaks at 232.65 and 235.56 eV to the Mo<sup>6+</sup> species [37,50–53]. The Mo<sup>4+</sup> and Mo<sup>6+</sup> peaks are associated with MoO<sub>2</sub> and MoO<sub>3</sub>, which stem from the unavoidable surface oxidation occurring when exposed to air [54]. In addition, the Mo 3d XPS spectra of Mo<sub>2</sub>C-Mo<sub>2</sub>N@CNW<sub>S</sub>/D-500, -750, -800, and -850 were recorded and deconvoluted using the similar doublets, as illustrated in Figure S13. Figure 4e presents a summary of the statistical percentage distribution of Mo species as the synthesis temperature varies. Mo<sub>2</sub>C-Mo<sub>2</sub>N@CNW<sub>S</sub>/D-500 possesses a higher percentage of Mo<sup>4+</sup> species than others, aligning with the distinct MoO<sub>2</sub> peak in the XRD result. Importantly, the percentage of the Mo-C bond generally increases from 13% to 53% with the temperature rising from 500 to 850 °C, while that of Mo-N bonds constantly remains around 33%. It is proposed that the high calcination temperature facilitates the transformation of the Mo-O (Mo<sup>4+</sup> and Mo<sup>6+</sup>) bonds into Mo-C bonds. Keep in mind that the Mo-C and Mo-N bonds are regarded as the active sites for HER [55]. To reveal the relative variation of these bonds, the ratio changes in Mo-C content ( $n(\text{Mo-C})$ ) to Mo-N content ( $n(\text{Mo-N})$ ) were determined in Figure 4f. One can see that the ratio progressively increases as a function of temperature, well in line with the XRD investigations (see Figures 4a and S10). Notably, it is the Mo<sub>2</sub>C-Mo<sub>2</sub>N@CNW<sub>S</sub>/D-650, with a ratio close

to 1 between Mo-C and Mo-N bonds, that demonstrates the lowest HER overpotential (and best HER performance) among these catalysts.

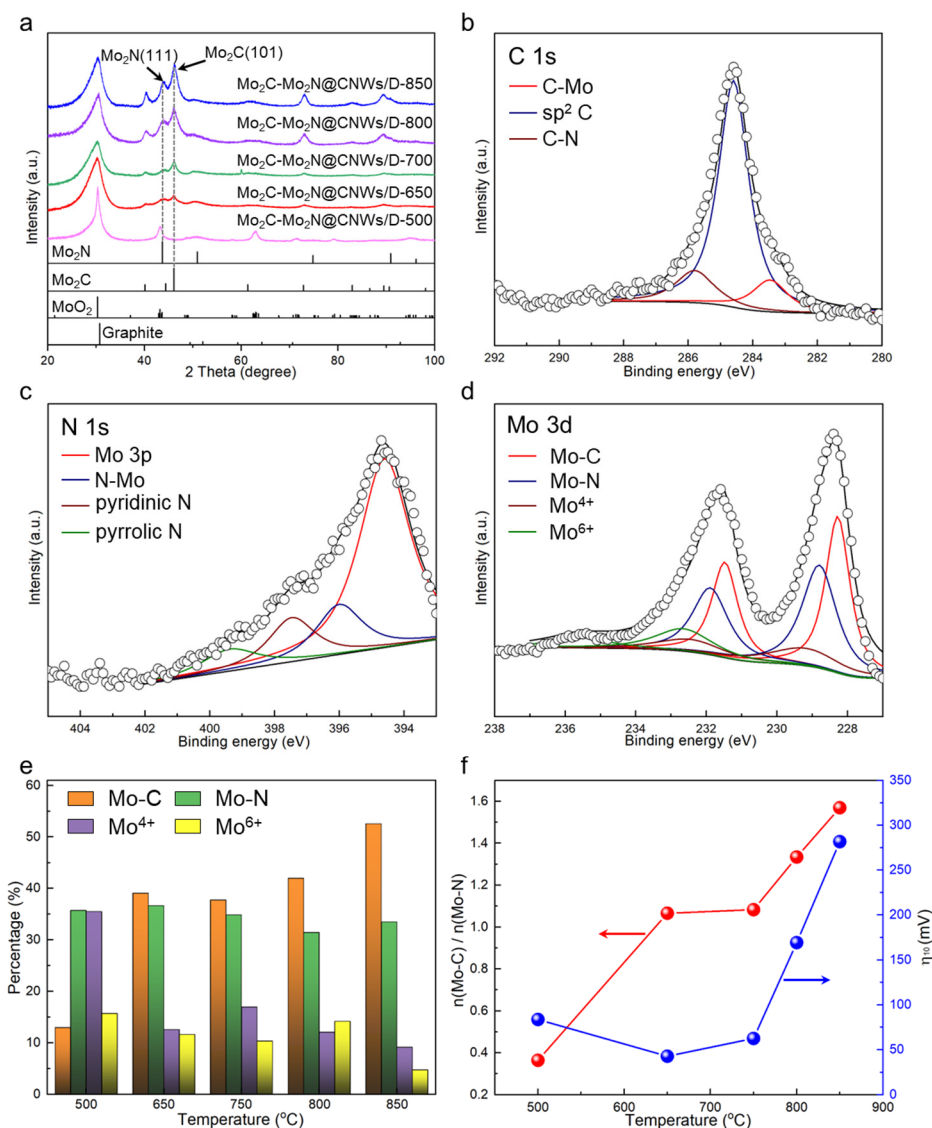


**Figure 4.** Constituent characterizations of Mo<sub>2</sub>C-Mo<sub>2</sub>N@CNWs/D. (a) XRD patterns of Mo<sub>2</sub>C-Mo<sub>2</sub>N@CNWs/D-500, -650, -700, -800, and -850. High-resolution XPS spectra and deconvoluted plots of (b) C 1s, (c) N 1s, and (d) Mo 3d in Mo<sub>2</sub>C-Mo<sub>2</sub>N@CNWs/D-650. (e) Histogram illustrating the statistical distribution of Mo species percentages and (f) the ratio of  $n(\text{Mo-C})/n(\text{Mo-N})$  derived from XPS deconvolution as a function of the temperature. The  $\eta_{10}$  variation with the temperature is also depicted in panel (f).

To further explore the synergistic effects involved in the HER activity on the Mo<sub>2</sub>C-Mo<sub>2</sub>N heterostructure, DFT calculations were carried out. Figure 5a exhibits the optimized atomic model of the Mo<sub>2</sub>N(111), Mo<sub>2</sub>C(101), and Mo<sub>2</sub>N(111)/Mo<sub>2</sub>C(101) heterostructure consistently well with XRD and TEM results. The possible adsorption sites of H<sup>\*</sup> are also indicated in the model. Figure 5b displays the free energy diagram ( $\Delta G_{\text{H}^*}$ ) of H<sup>\*</sup> adsorption/desorption on different electrocatalysts.  $\Delta G_{\text{H}^*}$  is supposed to be a significant indicator of the electrocatalyst activity. Regarding ideal  $\Delta G_{\text{H}^*}$ , it is hoped that it is close to zero since either a negative  $\Delta G_{\text{H}^*}$ , meaning the facile adsorption of H<sup>\*</sup> on the active site but challenging detachment, or a positive  $\Delta G_{\text{H}^*}$ , indicating the arduous attachment of H on the active site but easy release, results in a large overpotential during the HER

process [56]. As listed in Table S1, Mo<sub>2</sub>N and Mo<sub>2</sub>C have an exothermic  $\Delta G_{H^*}$ , calculated to be  $-0.5889$  and  $-0.3178$  eV, respectively, implying an impediment to hydrogen release and hence a poor HER performance. For the Mo<sub>2</sub>C-Mo<sub>2</sub>N heterostructure, the  $\Delta G_{H^*}$  values for HER occurring on the interfacial N, Mo (bonded with N and C atoms), and C site are  $0.0913$ ,  $-0.1673$ , and  $-0.6604$  eV, respectively. Therefore, interfacial N and Mo (bonded with N and C atoms) atoms are two major active centers for HER. More significantly, the  $|\Delta G_{H^*}|$  value of these centers is much closer to zero compared to those of Mo<sub>2</sub>N and Mo<sub>2</sub>C, which endows the desired balance between adsorption and desorption of H<sup>\*</sup>, contributing to a high electrocatalytic activity of the Mo<sub>2</sub>C-Mo<sub>2</sub>N heterostructure. To support such theoretical results, Mo<sub>2</sub>C@CNW<sub>5</sub>/D-650 was prepared on the CC without the melamine introduction (see XRD pattern in Figure S14). Figure S15 and Table S2 confirm the beneficial effect derived from the Mo<sub>2</sub>C-Mo<sub>2</sub>N heterostructure on the HER, because the Mo<sub>2</sub>C-Mo<sub>2</sub>N@CNW<sub>5</sub>/D-650 possesses a much smaller overpotential ( $\eta_{10} = 42.8$  mV) and lower Tafel slope ( $45.6$  mV/dec) than the Mo<sub>2</sub>C@CNW<sub>5</sub>/D-650 ( $\eta_{10} = 107.9$  mV, Tafel slope =  $52.9$  mV/dec).

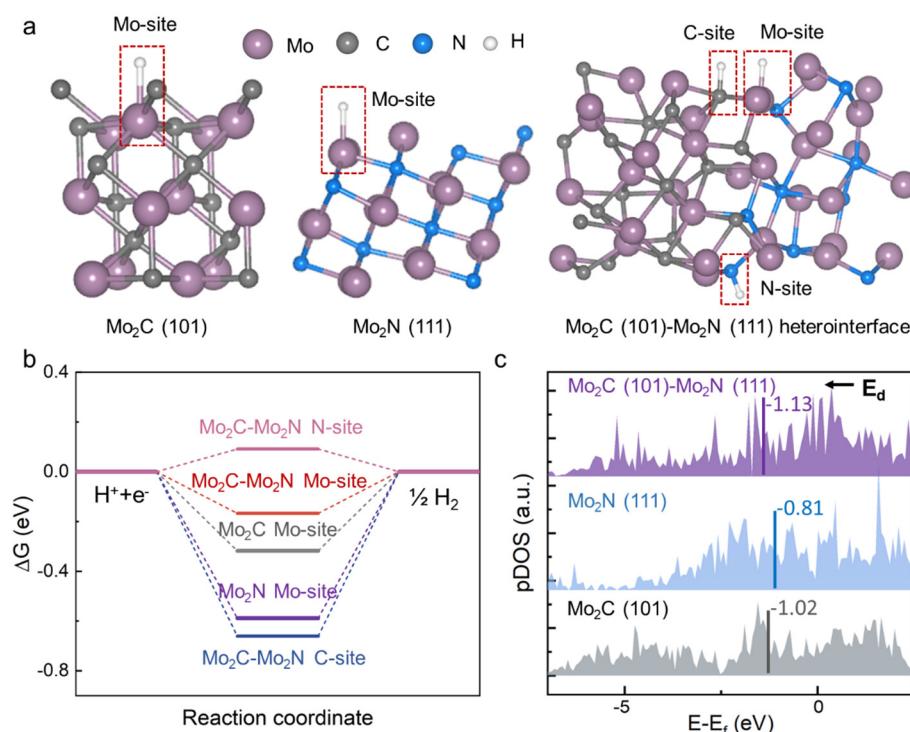


**Figure 5.** DFT calculations for HER energy variation and electronic states. (a) Optimized structural model with H<sup>\*</sup> adsorbable sites, (b) free energy diagram of H<sup>\*</sup> adsorption/desorption, and (c) partial density of states of Mo d orbitals for Mo<sub>2</sub>N (111) facet, Mo<sub>2</sub>C (101) facet, and Mo<sub>2</sub>C (101)-Mo<sub>2</sub>N (111) heterostructure. The Fermi level is referenced to 0 eV in panel (c).

To further explain the factors affecting the adsorption energy on the Mo<sub>2</sub>C-Mo<sub>2</sub>N heterostructure, we investigated the electronic states of Mo d orbitals and calculated the corresponding d-band center (Figure 5c). The heterostructure possesses a more negative d-band center ( $-1.13$  eV) than that of Mo<sub>2</sub>N ( $-0.81$  eV) and Mo<sub>2</sub>C ( $-1.02$  eV), indicating that the surplus H<sup>\*</sup> binding capacity favorably weakens, which thus contributes to a decreased  $|\Delta G_{H^*}|$  value on the interfacial Mo site of Mo<sub>2</sub>C-Mo<sub>2</sub>N [57], as explained in Figure 5b. In addition, the local density of state of Mo<sub>2</sub>C-Mo<sub>2</sub>N is higher than that of Mo<sub>2</sub>N and Mo<sub>2</sub>C near the Fermi level. Such enhancement facilitates a rapid charge transfer rate at the electrolyte(H<sup>+</sup>)/electrocatalyst interface in the HER, consistently supported by the much lower  $R_{ct}$  on the Mo<sub>2</sub>C-Mo<sub>2</sub>N ( $8.59 \Omega$ ) than Mo<sub>2</sub>C ( $129.42 \Omega$ ) in Table S2.

The fast charge transfer process further triggers a superior HER activity on the Mo<sub>2</sub>C-Mo<sub>2</sub>N heterostructure.

DFT calculation reveals that the interfacial atoms, particularly N and Mo atoms, take a pivotal role in determining the high intrinsic activity of the Mo<sub>2</sub>N-Mo<sub>2</sub>C heterostructure. Therefore, more interface sites are created, and more active HER performance will be harvested. Considering a constant total amount of Mo<sub>2</sub>N and Mo<sub>2</sub>C, and only the Mo<sub>2</sub>N content is equal to the Mo<sub>2</sub>C content, could the maximal interfacial abundance possibly be approached. That is why the utmost HER efficiency was observed when the ratio of  $n(\text{Mo-N})/n(\text{Mo-C})$  of Mo<sub>2</sub>C-Mo<sub>2</sub>N@CNWs/D-650 is close to 1, as shown in Figure 4f. In the study by Liu et al., the MoC-Mo<sub>2</sub>C heterostructure was developed as the HER electrocatalyst. They also uncovered that the optimum HER efficiency was attained when the MoC and Mo<sub>2</sub>C exhibited nearly identical concentrations.

Furthermore, 3D-networked CNWs/D possesses a high electrical conductivity, open accessible surface, and large surface area, working as an excellent current collector to efficiently promote the charge transfer on the active sites of porous Mo<sub>2</sub>C-Mo<sub>2</sub>N and enhance the overall high-current HER performance. Figure S16 and Table S2 display that the Mo<sub>2</sub>C-Mo<sub>2</sub>N@CNWs/D-650 has a close Tafel slope with the Mo<sub>2</sub>C-Mo<sub>2</sub>N@CC-650, indicating the nearly identical HER kinetics derived from the Mo<sub>2</sub>C-Mo<sub>2</sub>N heterostructure. Nevertheless, owing to more than a two-fold increase in capacitance (also ECSA) stemming from the CNWs/D, the Mo<sub>2</sub>C-Mo<sub>2</sub>N@CNWs/D-650 exhibits a much lower overpotential ( $\eta_{1000} = 194.4$  mV) than that of Mo<sub>2</sub>C-Mo<sub>2</sub>N@CC-650 ( $\eta_{1000} = 251.7$  mV).

In short, we constructed a highly active Mo<sub>2</sub>C-Mo<sub>2</sub>N heterointerface and augmented the abundance of interfacial sites through facilely manipulating the annealing temperature. This, coupled with the enhanced ECSA provided by the CNWs/D current collector, synergistically results in exceptional HER performance at high current densities.

#### 4. Conclusions

In summary, a binder-free Mo<sub>2</sub>C-Mo<sub>2</sub>N@CNWs/D heterostructure is facilely prepared via ultrasonically soaking in a Mo-salt solution followed by an annealing treatment and the outstanding performance is demonstrated using this self-supporting electrocatalyst in the high-current-density HER. The Mo<sub>2</sub>C-Mo<sub>2</sub>N@CNWs/D not only delivers a low overpotential of 42.8 mV at a small current density of 10 mA/cm<sup>2</sup> but also maintains impressively low overpotentials of 137.8 and 194.4 mV at high current densities of 500 and 1000 mA/cm<sup>2</sup>, respectively. The outstanding high-current HER performance could be ascribed to synergistic merits derived from the Mo<sub>2</sub>C-Mo<sub>2</sub>N heterostructure and CNWs/D as follows: (1) DFT calculations reveal that the heterojunction of Mo<sub>2</sub>C and Mo<sub>2</sub>N downshifts the d-band center of interfacial Mo orbitals, contributing to a  $\Delta G_{\text{H}^+}$  value that is close to zero, thus leading to high interfacial activity of Mo<sub>2</sub>C-Mo<sub>2</sub>N. (2) The hetero-interfacial active sites are enriched through elaborately manipulating the proportion of the Mo-C bond to Mo-N bond close to 1. (3) Benefitting from a high electrical conductivity, open accessible surface, and large surface area, the 3D-networked CNWs/D serves as a good current collector to facilitate the electron transfer occurring on the interfacial sites of Mo<sub>2</sub>C-Mo<sub>2</sub>N. This work highlights an effective way to design a highly active non-precious electrocatalyst and promises its applications in the electrochemical hydrogen production industry.

**Supplementary Materials:** The following supporting information can be downloaded at: <https://www.mdpi.com/article/10.3390/nano14030243/s1>, Figure S1: Side view (upper panel) and top view (lower panel) for model structures; Figure S2: SEM images of CC; Figure S3: SEM image and Raman spectrum of the CNW/D-coated CC; Figure S4: TEM images of Mo<sub>2</sub>C-Mo<sub>2</sub>N@CNWs/D; Figure S5: EDS spectrum of Mo<sub>2</sub>C-Mo<sub>2</sub>N@CNWs/D; Figure S6: Polarization curves of Mo<sub>2</sub>C-Mo<sub>2</sub>N@CNWs/D prepared at 700 °C with the annealing time; Figure S7: CV curves of Mo<sub>2</sub>C-Mo<sub>2</sub>N@CNWs/D at various scan rates; Figure S8: SEM image of Mo<sub>2</sub>C-Mo<sub>2</sub>N@CNWs/D-650 after a 24 h HER test; Figure S9. Raman spectra of Mo<sub>2</sub>C-Mo<sub>2</sub>N@CNWs/D; Figure S10: The intensity ratio of the Mo<sub>2</sub>C (101) peak to the Mo<sub>2</sub>N (111) peak in XRD patterns as a function of the temperature; Figure S11: XPS survey spectrum of Mo<sub>2</sub>C-Mo<sub>2</sub>N@CNWs/D-650; Figure S12: XPS survey spectrum

of Mo<sub>2</sub>C-Mo<sub>2</sub>N@CNWs/D-650 after HER test; Figure S13: High-resolution Mo 3d XPS spectra of Mo<sub>2</sub>C-Mo<sub>2</sub>N@CNWs/D; Figure S14: XRD pattern of Mo<sub>2</sub>C@CNWs/D-650; Figure S15: Electrocatalytic HER performance of Mo<sub>2</sub>C@CNWs/D-650; Figure S16: Electrocatalytic HER performance of Mo<sub>2</sub>C-Mo<sub>2</sub>N@CC-650; Table S1: The adsorption energy change in H<sup>+</sup> species ( $\Delta E_{H^+}$ ) and the free energy change in adsorbed H<sup>+</sup> species ( $\Delta G_{H^+}$ ); Table S2: Electrocatalytic HER characteristics of Mo<sub>2</sub>C@CNWs/D-650, Mo<sub>2</sub>C-Mo<sub>2</sub>N@CC-650, and Mo<sub>2</sub>C-Mo<sub>2</sub>N@CNWs/D-650.

**Author Contributions:** Conceptualization, Z.Z. (Zhaofeng Zhai), X.J. and N.H.; Methodology, Z.Z. (Zhaofeng Zhai), C.Z. and B.C.; Funding acquisition, Z.Z. (Zhaofeng Zhai), N.H. and L.L.; Investigation, Z.Z. (Zhaofeng Zhai), C.Z., B.C., H.S., Z.Z. (Ziwen Zheng), J.L., X.J. and N.H.; Writing—original draft and editing, Z.Z. (Zhaofeng Zhai); Data curation, C.Z.; Formal analysis, L.L. and B.Y.; Writing—review and editing, X.J. and N.H. All authors have read and agreed to the published version of the manuscript.

**Funding:** This work was funded by the National Natural Science Foundation of China (Grant No. 52202054 and No. 51202257), the IMR Innovation Fund (Grant No. 2021-PY14), the “Jie Bang Gua Shuai” Key Technologies R & D Program of Liaoning Province (No. 2021JH1/10400031), and the Technical Innovation Project for Functional Development of Instruments and Equipment of the Chinese Academy of Sciences (No. sjzx-gnkf-202203).

**Data Availability Statement:** The data presented in this study are available on request from the corresponding author.

**Acknowledgments:** We gratefully acknowledge funding support. We are grateful to the Shenzhen Cloud Computing Center for allowing the use of their computing facilities for DFT simulations.

**Conflicts of Interest:** The authors declare no conflicts of interest.

## References

1. Lagadee, M.F.; Grimaud, A. Water electrolyzers with closed and open electrochemical systems. *Nat. Mater.* **2020**, *19*, 1140–1150. [[CrossRef](#)] [[PubMed](#)]
2. Hu, K.; Ohto, T.; Nagata, Y.; Wakisaka, M.; Aoki, Y.; Fujita, J.I.; Ito, Y. Catalytic activity of graphene-covered non-noble metals governed by proton penetration in electrochemical hydrogen evolution reaction. *Nat. Commun.* **2021**, *12*, 203. [[CrossRef](#)] [[PubMed](#)]
3. Shen, Y.; Zhou, Y.; Wang, D.; Wu, X.; Li, J.; Xi, J. Nickel-copper alloy encapsulated in graphitic carbon shells as electrocatalysts for hydrogen evolution reaction. *Adv. Energy Mater.* **2018**, *8*, 1701759. [[CrossRef](#)]
4. Liu, Y.; Yu, G.; Li, G.-D.; Sun, Y.; Asefa, T.; Chen, W.; Zou, X. Coupling Mo<sub>2</sub>C with nitrogen-rich nanocarbon leads to efficient hydrogen-evolution electrocatalytic sites. *Angew. Chem.-Int. Ed.* **2015**, *54*, 10752–10757. [[CrossRef](#)]
5. Li, J.-S.; Wang, Y.; Liu, C.-H.; Li, S.-L.; Wang, Y.-G.; Dong, L.-Z.; Dai, Z.-H.; Li, Y.-F.; Lan, Y.-Q. Coupled molybdenum carbide and reduced graphene oxide electrocatalysts for efficient hydrogen evolution. *Nat. Commun.* **2016**, *7*, 11204. [[CrossRef](#)] [[PubMed](#)]
6. Chen, Y.; Yu, G.; Chen, W.; Liu, Y.; Li, G.-D.; Zhu, P.; Tao, Q.; Li, Q.; Liu, J.; Shen, X.; et al. Highly active, nonprecious electrocatalyst comprising borophene subunits for the hydrogen evolution reaction. *J. Am. Chem. Soc.* **2017**, *139*, 12370–12373. [[CrossRef](#)] [[PubMed](#)]
7. Li, S.; Li, E.; An, X.; Hao, X.; Jiang, Z.; Guan, G. Transition metal-based catalysts for electrochemical water splitting at high current density: Current status and perspectives. *Nanoscale* **2021**, *13*, 12788–12817. [[CrossRef](#)]
8. Chi, J.-Q.; Yang, M.; Chai, Y.-M.; Yang, Z.; Wang, L.; Dong, B. Design and modulation principles of molybdenum carbide-based materials for green hydrogen evolution. *J. Energy Chem.* **2020**, *48*, 398–423. [[CrossRef](#)]
9. Ledendecker, M.; Mondschein, J.S.; Kasian, O.; Geiger, S.; Göhl, D.; Schalenbach, M.; Zeradjanin, A.; Cherevko, S.; Schaak, R.E.; Mayrhofer, K. Stability and activity of non-noble-metal-based catalysts toward the hydrogen evolution reaction. *Angew. Chem.-Int. Ed.* **2017**, *56*, 9767–9771. [[CrossRef](#)]
10. Kitchin, J.R.; Nørskov, J.K.; Barteau, M.A.; Chen, J.G. Trends in the chemical properties of early transition metal carbide surfaces: A density functional study. *Catal. Today* **2005**, *105*, 66–73. [[CrossRef](#)]
11. Liu, Y.; Huo, J.; Guo, J.; Lu, L.; Shen, Z.; Chen, W.; Liu, C.; Liu, H. Hierarchical porous molybdenum carbide based nanomaterials for electrocatalytic hydrogen production. *Front. Chem.* **2020**, *8*, 426. [[CrossRef](#)] [[PubMed](#)]
12. Michalsky, R.; Zhang, Y.-J.; Peterson, A.A. Trends in the hydrogen evolution activity of metal carbide catalysts. *ACS Catal.* **2014**, *4*, 1274–1278. [[CrossRef](#)]
13. Kim, S.; Choi, C.; Hwang, J.; Park, J.; Jeong, J.; Jun, H.; Lee, S.; Kim, S.-K.; Jang, J.H.; Jung, Y.; et al. Interaction mediator assisted synthesis of mesoporous molybdenum carbide: Mo-valence state adjustment for optimizing hydrogen evolution. *ACS Nano* **2020**, *14*, 4988–4999. [[CrossRef](#)] [[PubMed](#)]

14. Chi, J.-Q.; Gao, W.-K.; Lin, J.-H.; Dong, B.; Qin, J.-F.; Liu, Z.-Z.; Liu, B.; Chai, Y.-M.; Liu, C.-G. Porous core-shell N-doped Mo<sub>2</sub>C@C nanospheres derived from inorganic-organic hybrid precursors for highly efficient hydrogen evolution. *J. Catal.* **2018**, *360*, 9–19. [[CrossRef](#)]
15. Jia, J.; Xiong, T.; Zhao, L.; Wang, F.; Liu, H.; Hu, R.; Zhou, J.; Zhou, W.; Chen, S. Ultrathin N-doped Mo<sub>2</sub>C nanosheets with exposed active sites as efficient electrocatalyst for hydrogen evolution reactions. *ACS Nano* **2017**, *11*, 12509–12518. [[CrossRef](#)]
16. Shi, Z.; Nie, K.; Shao, Z.-J.; Gao, B.; Lin, H.; Zhang, H.; Liu, B.; Wang, Y.; Zhang, Y.; Sun, X.; et al. Phosphorus-Mo<sub>2</sub>C@carbon nanowires toward efficient electrochemical hydrogen evolution: Composition, structural and electronic regulation. *Energy Environ. Sci.* **2017**, *10*, 1262–1271. [[CrossRef](#)]
17. Xiong, K.; Li, L.; Zhang, L.; Ding, W.; Peng, L.; Wang, Y.; Chen, S.; Tan, S.; Wei, Z. Ni-doped Mo<sub>2</sub>C nanowires supported on Ni foam as a binder-free electrode for enhancing the hydrogen evolution performance. *J. Mater. Chem. A* **2015**, *3*, 1863–1867. [[CrossRef](#)]
18. Lin, H.; Liu, N.; Shi, Z.; Guo, Y.; Tang, Y.; Gao, Q. Cobalt-doping in molybdenum-carbide nanowires toward efficient electrocatalytic hydrogen evolution. *Adv. Funct. Mater.* **2016**, *26*, 5590–5598. [[CrossRef](#)]
19. Liu, W.; Wang, X.; Wang, F.; Du, K.; Zhang, Z.; Guo, Y.; Yin, H.; Wang, D. A durable and pH-universal self-standing MoC-Mo<sub>2</sub>C heterojunction electrode for efficient hydrogen evolution reaction. *Nat. Commun.* **2021**, *12*, 6776. [[CrossRef](#)]
20. Li, C.; Wang, Z.; Liu, M.; Wang, E.; Wang, B.; Xu, L.; Jiang, K.; Fan, S.; Sun, Y.; Li, J.; et al. Ultrafast self-heating synthesis of robust heterogeneous nanocarbides for high current density hydrogen evolution reaction. *Nat. Commun.* **2022**, *13*, 3338. [[CrossRef](#)]
21. Yan, H.; Xie, Y.; Jiao, Y.; Wu, A.; Tian, C.; Zhang, X.; Wang, L.; Fu, H. Holey reduced graphene oxide coupled with an Mo<sub>2</sub>N-Mo<sub>2</sub>C heterojunction for efficient hydrogen evolution. *Adv. Mater.* **2018**, *30*, 1704156. [[CrossRef](#)] [[PubMed](#)]
22. Zhang, B.; Xu, H.; Chen, Q.; Chen, H.; He, G. ZIF-67 derived Mo<sub>2</sub>N/Mo<sub>2</sub>C heterostructure as high-efficiency electrocatalyst for hydrogen evolution reaction. *J. Alloys Compd.* **2022**, *922*, 166216. [[CrossRef](#)]
23. Song, H.; Guo, S.; Zhang, X.; Yang, Y.; Gao, B.; Pi, Y.; Pi, C.; Chu, P.K.; Huo, K. In-situ and controllable construction of Mo<sub>2</sub>N embedded Mo<sub>2</sub>C nanobelts as robust electrocatalyst for superior pH-universal hydrogen evolution reaction. *J. Alloys Compd.* **2022**, *918*, 165611. [[CrossRef](#)]
24. Xia, M.; Li, S.; Zhang, X.; Xie, Z. Guanosine-assisted synthesis of a core-shell Mo<sub>2</sub>N/Mo<sub>2</sub>C/C structure for enhanced hydrogen evolution reaction. *Inorg. Chem. Front.* **2023**, *10*, 7018–7027. [[CrossRef](#)]
25. Bang, J.; Moon, I.K.; Kim, Y.-K.; Oh, J. Heterostructured Mo<sub>2</sub>N-Mo<sub>2</sub>C nanoparticles coupled with N-doped carbonized wood to accelerate the hydrogen evolution reaction. *Small Struct.* **2023**, *4*, 2200283. [[CrossRef](#)]
26. Shi, H.; Dai, T.Y.; Wan, W.B.; Wen, Z.; Lang, X.Y.; Jiang, Q. Mo-/Co-N-C hybrid nanosheets oriented on hierarchical nanoporous Cu as versatile electrocatalysts for efficient water splitting. *Adv. Funct. Mater.* **2021**, *31*, 2102285. [[CrossRef](#)]
27. Greczynski, G.; Hultman, L. A Step-by-Step Guide to Perform X-ray Photoelectron Spectroscopy. *J. Appl. Phys.* **2022**, *132*, 11101. [[CrossRef](#)]
28. Wang, V.; Xu, N.; Liu, J.-C.; Tang, G.; Geng, W.-T. Vaspkit: A user-friendly interface facilitating high-throughput computing and analysis using vasp code. *Comput. Phys. Commun.* **2021**, *267*, 108033. [[CrossRef](#)]
29. Le, H.T.; Tran, D.T.; Kim, N.H.; Lee, J.H. Worm-Like Gold Nanowires Assembled Carbon Nanofibers-CVD Graphene Hybrid as Sensitive and Selective Sensor for Nitrite Detection. *J. Colloid Interface Sci.* **2021**, *583*, 425–434. [[CrossRef](#)]
30. Kim, H.; Huang, X.; Guo, X.; Wang, Y.; Cui, S.; Wen, Z.; Chen, J. Novel Hybrid Si Film/Highly Branched Graphene Nanosheets for Anode Materials in Lithium-Ion Batteries. *J. Phys. D-Appl. Phys.* **2019**, *52*, 345201. [[CrossRef](#)]
31. Zhai, Z.; Leng, B.; Yang, N.; Yang, B.; Liu, L.; Huang, N.; Jiang, X. Rational construction of 3D-networked carbon nanowalls/diamond supporting CuO architecture for high-performance electrochemical biosensors. *Small* **2019**, *15*, 1901527. [[CrossRef](#)] [[PubMed](#)]
32. Jansonius, R.P.; Schauer, P.A.; Dvorak, D.J.; MacLeod, B.P.; Fork, D.K.; Berlinguette, C.P. Strain influences the hydrogen evolution activity and absorption capacity of palladium. *Angew. Chem.-Int. Ed.* **2020**, *59*, 12192–12198. [[CrossRef](#)] [[PubMed](#)]
33. Xue, S.; Liu, Z.; Ma, C.; Cheng, H.-M.; Ren, W. A highly active and durable electrocatalyst for large current density hydrogen evolution reaction. *Sci. Bull.* **2020**, *65*, 123–130. [[CrossRef](#)] [[PubMed](#)]
34. Zhang, X.; Wang, J.; Guo, T.; Liu, T.; Wu, Z.; Cavallo, L.; Cao, Z.; Wang, D. Structure and phase regulation in Mo<sub>x</sub>C (alpha-MoC<sub>1-x</sub>/beta-Mo<sub>2</sub>C) to enhance hydrogen evolution. *Appl. Catal. B-Environ.* **2019**, *247*, 78–85. [[CrossRef](#)]
35. Zhai, Z.; Huang, N.; Zhuang, H.; Liu, L.; Yang, B.; Wang, C.; Gai, Z.; Guo, F.; Li, Z.; Jiang, X. A diamond/graphite nanoplatelets electrode for anodic stripping voltammetric trace determination of Zn(II), Cd(II), Pb(II) and Cu(II). *Appl. Surf. Sci.* **2018**, *457*, 1192–1201. [[CrossRef](#)]
36. Gu, Y.; Wu, A.; Jiao, Y.; Zheng, H.; Wang, X.; Xie, Y.; Wang, L.; Tian, C.; Fu, H. Two-dimensional porous molybdenum phosphide/nitride heterojunction nanosheets for pH-universal hydrogen evolution reaction. *Angew. Chem.-Int. Ed.* **2021**, *60*, 6673–6681. [[CrossRef](#)]
37. Luo, Y.; Tang, L.; Khan, U.; Yu, Q.; Cheng, H.-M.; Zou, X.; Liu, B. Morphology and surface chemistry engineering toward pH-universal catalysts for hydrogen evolution at high current density. *Nat. Commun.* **2019**, *10*, 269. [[CrossRef](#)]
38. Sun, H.; Xu, X.; Yan, Z.; Chen, X.; Jiao, L.; Cheng, F.; Chen, J. Superhydrophilic amorphous Co-B-P nanosheet electrocatalysts with Pt-like activity and durability for the hydrogen evolution reaction. *J. Mater. Chem. A* **2018**, *6*, 22062–22069. [[CrossRef](#)]

39. Yu, X.; Yu, Z.-Y.; Zhang, X.-L.; Zheng, Y.-R.; Duan, Y.; Gao, Q.; Wu, R.; Sun, B.; Gao, M.-R.; Wang, G.; et al. "Superaerophobic" nickel phosphide nanoarray catalyst for efficient hydrogen evolution at ultrahigh current densities. *J. Am. Chem. Soc.* **2019**, *141*, 7537–7543. [[CrossRef](#)]
40. Yu, L.; Mishra, I.K.; Xie, Y.; Zhou, H.; Sun, J.; Zhou, J.; Ni, Y.; Luo, D.; Yu, F.; Yu, Y.; et al. Ternary Ni<sub>2(1-x)</sub>Mo<sub>2x</sub>P nanowire arrays toward efficient and stable hydrogen evolution electrocatalysis under large-current-density. *Nano Energy* **2018**, *53*, 492–500. [[CrossRef](#)]
41. Huang, C.; Yu, L.; Zhang, W.; Xiao, Q.; Zhou, J.; Zhang, Y.; An, P.; Zhang, J.; Yu, Y. N-doped Ni-Mo based sulfides for high-efficiency and stable hydrogen evolution reaction. *Appl. Catal. B-Environ.* **2020**, *276*, 119137. [[CrossRef](#)]
42. Wang, Z.; Chen, J.; Song, E.; Wang, N.; Dong, J.; Zhang, X.; Ajayan, P.M.; Yao, W.; Wang, C.; Liu, J.; et al. Manipulation on active electronic states of metastable phase  $\beta$ -NiMoO<sub>4</sub> for large current density hydrogen evolution. *Nat. Commun.* **2021**, *12*, 5960. [[CrossRef](#)] [[PubMed](#)]
43. Wang, L.; Cao, J.; Lei, C.; Dai, Q.; Yang, B.; Li, Z.; Zhang, X.; Yuan, C.; Lei, L.; Hou, Y. Strongly coupled 3D N-doped MoO<sub>2</sub>/Ni<sub>3</sub>S<sub>2</sub> hybrid for high current density hydrogen evolution electrocatalysis and biomass upgrading. *ACS Appl. Mater. Interfaces* **2019**, *11*, 27743–27750. [[CrossRef](#)]
44. Pei, Y.; Huang, L.; Han, L.; Zhang, H.; Dong, L.; Jia, Q.; Zhang, S. NiCoP/NiOOH nanoflowers loaded on ultrahigh porosity Co foam for hydrogen evolution reaction under large current density. *Green Energy Environ.* **2022**, *7*, 467–476. [[CrossRef](#)]
45. Parvin, S.; Kumar, A.; Ghosh, A.; Bhattacharyya, S. An earth-abundant bimetallic catalyst coated metallic nanowire grown electrode with platinum-like pH-universal hydrogen evolution activity at high current density. *Chem. Sci.* **2020**, *11*, 3893–3902. [[CrossRef](#)] [[PubMed](#)]
46. Zhu, W.; Chen, W.; Yu, H.; Zeng, Y.; Ming, F.; Liang, H.; Wang, Z. NiCo/NiCo-OH and NiFe/NiFe-OH core shell nanostructures for water splitting electrocatalysis at large currents. *Appl. Catal. B-Environ.* **2020**, *278*, 119326. [[CrossRef](#)]
47. Yang, H.; Chen, Z.; Guo, P.; Fei, B.; Wu, R. B-doping-induced amorphization of LDH for large-current-density hydrogen evolution reaction. *Appl. Catal. B-Environ.* **2020**, *261*, 118240. [[CrossRef](#)]
48. Liu, Y.; Dou, Y.; Li, S.; Xia, T.; Xie, Y.; Wang, Y.; Zhang, W.; Wang, J.; Huo, L.; Zhao, H. Synergistic interaction of double/simple perovskite heterostructure for efficient hydrogen evolution reaction at high current density. *Small Methods* **2021**, *5*, 2000701. [[CrossRef](#)]
49. Li, P.; Wu, D.; Dai, C.; Huang, X.; Li, C.; Yin, Z.; Zhou, S.; Lv, Z.; Cheng, D.; Zhu, J.; et al. Controlled synthesis of copper-doped molybdenum carbide catalyst with enhanced activity and stability for hydrogen evolution reaction. *Catal. Lett.* **2019**, *149*, 1368–1374. [[CrossRef](#)]
50. Li, S.; Cheng, C.; Sagaltchik, A.; Pachfule, P.; Zhao, C.; Thomas, A. Metal-organic precursor-derived mesoporous carbon spheres with homogeneously distributed molybdenum carbide/nitride nanoparticles for efficient hydrogen evolution in alkaline media. *Adv. Funct. Mater.* **2019**, *29*, 1807419. [[CrossRef](#)]
51. Wei, Z.B.Z.; Grange, P.; Delmon, B. XPS and XRD studies of fresh and sulfided Mo<sub>2</sub>N. *Appl. Surf. Sci.* **1998**, *135*, 107–114. [[CrossRef](#)]
52. Wei, H.; Xi, Q.; Chen, X.; Guo, D.; Ding, F.; Yang, Z.; Wang, S.; Li, J.; Huang, S. Molybdenum carbide nanoparticles coated into the graphene wrapping N-doped porous carbon microspheres for highly efficient electrocatalytic hydrogen evolution both in acidic and alkaline media. *Adv. Sci.* **2018**, *5*, 1700733. [[CrossRef](#)] [[PubMed](#)]
53. Han, W.; Chen, L.; Ma, B.; Wang, J.; Song, W.; Fan, X.; Li, Y.; Zhang, F.; Peng, W. Ultra-small Mo<sub>2</sub>C nanodots encapsulated in nitrogen-doped porous carbon for pH-universal hydrogen evolution: Insights into the synergistic enhancement of her activity by nitrogen doping and structural defects. *J. Mater. Chem. A* **2019**, *7*, 4734–4743. [[CrossRef](#)]
54. Li, H.; Hu, M.; Zhang, L.; Huo, L.; Jing, P.; Liu, B.; Gao, R.; Zhang, J.; Liu, B. Hybridization of bimetallic molybdenum-tungsten carbide with nitrogen-doped carbon: A rational design of super active porous composite nanowires with tailored electronic structure for boosting hydrogen evolution catalysis. *Adv. Funct. Mater.* **2020**, *30*, 2003198. [[CrossRef](#)]
55. Ma, R.; Zhou, Y.; Chen, Y.; Li, P.; Liu, Q.; Wang, J. Ultrafine molybdenum carbide nanoparticles composited with carbon as a highly active hydrogen-evolution electrocatalyst. *Angew. Chem.-Int. Ed.* **2015**, *54*, 14723–14727. [[CrossRef](#)]
56. Seh, Z.W.; Kibsgaard, J.; Dickens, C.F.; Chorkendorff, I.; Nørskov, J.K.; Jaramillo, T.F. Combining theory and experiment in electrocatalysis: Insights into materials design. *Science* **2017**, *355*, eaad4998. [[CrossRef](#)]
57. Zhang, C.; Huang, N.; Zhai, Z.; Liu, L.; Chen, B.; Yang, B.; Jiang, X.; Yang, N. Bifunctional oxygen electrocatalyst of Co<sub>4</sub>N and nitrogen-doped carbon nanowalls/diamond for high-performance flexible zinc-air batteries. *Adv. Energy Mater.* **2023**, *13*, 2301749. [[CrossRef](#)]

**Disclaimer/Publisher's Note:** The statements, opinions and data contained in all publications are solely those of the individual author(s) and contributor(s) and not of MDPI and/or the editor(s). MDPI and/or the editor(s) disclaim responsibility for any injury to people or property resulting from any ideas, methods, instructions or products referred to in the content.